

## COSMIC SHEAR STATISTICS IN THE SUPRIME-CAM 2.1 SQ DEG FIELD: CONSTRAINTS ON $\Omega_M$ AND $\sigma_8$ <sup>1</sup>

TAKASHI HAMANA<sup>2,3</sup>, SATOSHI MIYAZAKI<sup>2</sup>, KAZUHIRO SHIMASAKU<sup>4</sup>, HISANORI FURUSAWA<sup>2</sup>, MAMORU DOI<sup>5</sup>, MASARU HAMABE<sup>6</sup>, KATSUMI IMI<sup>6</sup>, MASAHIKO KIMURA<sup>8</sup>, YUTAKA KOMIYAMA<sup>2</sup>, FUMIAKI NAKATA<sup>2</sup>, NORIO OKADA<sup>2</sup>, SADANORI OKAMURA<sup>4</sup>, MASAMI OUCHI<sup>4</sup>, MAKI SEKIGUCHI<sup>8</sup>, MASAFUMI YAGI<sup>2</sup> AND NAOKI YASUDA<sup>2</sup>  
hamana@iap.fr

Submitted to ApJ; Draft version November 10, 2018

### ABSTRACT

We present measurements of the cosmic shear correlation in the shapes of galaxies in the Suprime-Cam 2.1 deg<sup>2</sup>  $R_c$ -band imaging data. As an estimator of the shear correlation originated from the gravitational lensing, we adopt the aperture mass variance, which most naturally decomposes the correlation signal into E and B (non-gravitational lensing) modes. We detect a non-zero E mode variance on scales between  $\theta_{ap} = 2'$  and  $40'$ . We also detect a small but non-zero B mode variance on scales larger than  $\theta_{ap} > 5'$ . We compare the measured E mode variance to the model predictions in CDM cosmologies using maximum likelihood analysis. A four-dimensional space is explored, which examines  $\sigma_8$ ,  $\Omega_m$ ,  $\Gamma$  (the shape parameter of the CDM power spectrum) and  $\bar{z}_s$  (a mean redshift of galaxies). We include three possible sources of error: statistical noise, the cosmic variance estimated using numerical experiments, and a residual systematic effect estimated from the B mode variance. We derive joint constraints on two parameters by marginalizing over the two remaining parameters. We obtain an upper limit of  $\Gamma < 0.5$  for  $\bar{z}_s > 0.9$  (68% confidence). For a prior  $\Gamma \in [0.1, 0.4]$  and  $\bar{z}_s \in [0.6, 1.4]$ , we find  $\sigma_8 = (0.50_{-0.16}^{+0.35})\Omega_m^{-0.37}$  for  $\Omega_m + \Omega_\Lambda = 1$  and  $\sigma_8 = (0.51_{-0.16}^{+0.29})\Omega_m^{-0.34}$  for  $\Omega_\Lambda = 0$  (95% confidence). If we take the currently popular  $\Lambda$ CDM model ( $\Omega_m = 0.3$ ,  $\Omega_\Lambda = 0.7$ ,  $\Gamma = 0.21$ ), we obtain a one-dimensional confidence interval on  $\sigma_8$  for the 95.4% level,  $0.62 < \sigma_8 < 1.32$  for  $\bar{z}_s \in [0.6, 1.4]$ . Information on the redshift distribution of galaxies is key to obtaining a correct cosmological constraint. An independent constraint on  $\Gamma$  from other observations is useful to tighten the constraint.

*Subject headings:* cosmology: observations — cosmological parameters — dark matter — gravitational lensing

### 1. INTRODUCTION

Cosmic shear, that is coherent distortions in distant galaxy images resulting from weak gravitational lensing by large-scale structures, has been recognized as a powerful tool for cosmology because it directly probes matter distribution regardless of any relation between mass and light (for reviews see, Mellier 1999, Bartelmann & Schneider 2001). Since the first reports of the detection of cosmic shear correlations (Van Waerbeke et al., 2000; Witteman et al., 2000; Bacon, Refregier & Ellis 2000; Kaiser, Wilson & Luppino 2000; Maoli et al. 2001; ), cosmic shear statistics have become a promising probe of cosmological parameters. Indeed, recent measurements of cosmic shear correlation have put useful constraints on the matter density parameter  $\Omega_m$  and the matter power spectrum normalization  $\sigma_8$  (Maoli et al. 2001; Bacon et al. 2002; Van Waerbeke et al. 2001; 2002; Hoekstra et al. 2002a; Hoekstra, Yee & Gladders 2002b; Brown et al. 2003; Jarvis et al. 2003). As the cosmic shear correlation is primarily sensitive to density fluctuation at intermediate redshifts ( $0.2 < z < 0.7$ ) and on scales from quasi-linear to nonlinear ( $1 < \theta < 50$  arcmin corresponding to comoving scales of  $0.38 < r < 19.2h^{-1}$ Mpc at  $z = 0.5$  for a cosmological model with  $\Omega_m = 0.3$  and  $\Omega_\Lambda = 0.7$ ), it provides cosmological

information that is independent of other observations, such as galaxy clustering, cluster number counts, and the cosmic microwave background anisotropies, and thus is complementary to these techniques.

Cosmic shear measurement is not an easy task; it requires a rigorous observation strategy, specifically, a deep and wide-field survey with very high image quality. A large number density of distant galaxies, ideally  $n_g > 30\text{arcmin}^{-2}$ , is needed to suppress random noise due to the intrinsic galaxy ellipticity. A wide survey area is necessary for suppression of the cosmic variance. In addition, good seeing conditions are essential for precise measurements of a galaxy's shape. Suprime-Cam, a wide-field camera mounted on the prime focus of the 8.2-m Subaru telescope, is an almost ideal camera for a weak lensing survey. It has a field of view of  $34' \times 27'$  with  $0''.202 \text{ pixel}^{-1}$ . The median seeing in the  $I_c$  band, monitored over a period of one-and-a-half years, is reported to be  $\sim 0.6$  arcsec (Miyazaki et al. 2002b). Subaru's light-gathering power enables a complete magnitude of  $R_C = 25.2$  (the turn-around of galaxy counts) to be obtained by a 30-min exposure, which provides a galaxy number density of  $n_g \sim 33\text{arcmin}^{-2}$ , after object selection (see §3). These advantages allow a weak lensing survey to be car-

<sup>1</sup> Based on data collected at Subaru Telescope, which is operated by the National Astronomical Observatory of Japan.

<sup>2</sup> National Astronomical Observatory of Japan, Mitaka, Tokyo 181-8588, Japan

<sup>3</sup> Institut d'Astrophysique de Paris, 98bis Boulevard Arago, F 75014 Paris, France

<sup>4</sup> Department of Astronomy, University of Tokyo, Bunkyo, Tokyo 113-0033, Japan

<sup>5</sup> Institute of Astronomy, University of Tokyo, Mitaka, Tokyo 181-0015, Japan

<sup>6</sup> Department of Mathematical and Physical Sciences, Japan Women's University, Bunkyo, Tokyo 112-8681, Japan

<sup>7</sup> Communication Network Center (Tsu-den), Mitsubishi Electric, Amagasaki, Hyogo 661-8661, Japan

<sup>8</sup> Institute for Cosmic Ray Research, University of Tokyo, Kashiwa, Chiba 277-8582, Japan

ried out efficiently.

In this paper we present the results of our analysis of  $R_c$ -band imaging data from a Suprime-Cam 2.1 deg<sup>2</sup> field. This field is composed of nine pointings in a  $3 \times 3$  mosaic configuration which covers a contiguous  $1.64^\circ \times 1.28^\circ$  area. A great advantage of these data is their very good and homogeneous image quality over the whole field, which allows us to obtain secure weak lensing measurements. These data were also used for the first halo number counts using the weak lensing technique (Miyazaki et al., 2002a), which demonstrated that a weak lensing halo survey is indeed a promising way to study the distribution and evolution of large-scale structures. In this paper, we concentrate on the measurement of cosmic shear correlations caused by large-scale structures. We carry out a full maximum likelihood analysis of the cosmic shear correlation over four parameters,  $\Omega_m$ ,  $\sigma_8$ ,  $\Gamma$  (a shape parameter of the Cold Dark Matter power spectrum) and  $\bar{z}_s$  (the mean redshift of the source galaxy distribution). We derive joint constraints on two parameters by marginalizing over the two remaining parameters, and obtain a constraint on  $\Omega_m$  and  $\sigma_8$ . We also obtain an upper limit on  $\Gamma$ . Confidence intervals on  $\sigma_8$  for the currently popular  $\Lambda$ CDM model ( $\Omega_m = 0.3$ ,  $\Omega_\Lambda = 0.7$  and  $\Gamma = 0.21$ ) are also derived.

The outline of this paper is as follows. In §2 we briefly discuss the theory of cosmic shear statistics and summarize the analytical formulas that are used to compute the theoretical predictions. Details of the observations and data are described in §3. A galaxy shape analysis is presented in §4. Measurement of the cosmic shear correlation is presented in §5. The measured cosmic shear correlation signal is compared with the theoretical prediction using maximum likelihood analysis in §6. Finally, §7 presents a summary and discussion. In the Appendix, we discuss tests of the anisotropic point spread function correction procedure in some detail.

## 2. BASICS OF COSMIC SHEAR CORRELATION

In this section, we provide a basic description of the theory of the cosmic shear correlation (see the reviews by Mellier 1999; Bartelmann & Schneider 2001 for details).

The observable shear two-point statistics can be related to the convergence power spectrum defined by

$$P_\kappa(l) = \frac{9\Omega_m^2}{4} \left(\frac{H_0}{c}\right)^4 \int_0^{\chi_H} d\chi \left[\frac{W(\chi)}{a(\chi)}\right]^2 P_\delta\left[\frac{l}{f_K(\chi)}; \chi\right], \quad (1)$$

where  $H_0$  is the Hubble parameter,  $\chi$  is the radial comoving distance,  $\chi_H$  corresponds to the horizon,  $a(\chi)$  is the scale factor and  $f_K(\chi)$  is the comoving angular diameter distance.  $P_\delta(k)$  is the matter power spectrum, for which we adopt the fitting function of the CDM power spectrum given by Bardeen et al. (1986), but we treat the shape parameter,  $\Gamma$ , as a free parameter. To take into account the effect of nonlinear growth of the density field, which has a significant impact on the shear correlation function on scales below one degree (Jain & Seljak 1997), we use the fitting function of Peacock & Dodds (1996).  $W(\chi)$  is the source weighted distance ratio given by,

$$W(\chi) = \int_\chi^{\chi_H} d\chi' n_s(\chi') \frac{f_K(\chi' - \chi)}{f_K(\chi)}, \quad (2)$$

here  $n_s(\chi)$  is the normalized redshift distribution of source galaxies, which we discuss later (§6.1).

Several real space estimators of the shear correlation have been proposed, including: the shear two-point correlation function (Blandford et al. 1991; Miralda-Escude 1991; Kaiser

1992), the top-hat shear variance (Bernardeau, Van Waerbeke & Mellier 1997) and the aperture mass variance (Schneider et al. 1998). For our maximum likelihood analysis, we adopt the aperture mass variance, which has the very useful property that it naturally carries out E/B mode decomposition (Schneider et al. 1998; Crittenden et al. 2002; Pen, Van Waerbeke & Mellier 2002). As gravitational lensing produces only E mode shear, E/B mode decomposition allows contamination from B mode shear (which is not caused by gravitational lensing) to be suppressed, and the amplitude of the B mode variance can be used to estimate the amplitude of the systematic error. The aperture mass is defined by

$$M_{ap} = \int d^2\theta U(\theta)\kappa(\theta), \quad (3)$$

where  $\kappa(\theta)$  is the lensing convergence field, and  $U(\theta)$  is the compensated filter, for which we adopt the following function proposed by Schneider et al. (1998)

$$U(\theta) = \frac{9}{\pi\theta_{ap}^2} \left(1 - \frac{\theta^2}{\theta_{ap}^2}\right) \left(\frac{1}{3} - \frac{\theta^2}{\theta_{ap}^2}\right), \quad (4)$$

for  $\theta < \theta_{ap}$ , and 0 otherwise. It should be emphasized that this filter probes an effective scale of  $\theta_{ap}/5$  not  $\theta_{ap}$ . The aperture mass can be calculated directly from the tangential shear  $\gamma_t$  (the tangential component of shear defined in the local frame connecting the aperture center to a galaxy), without the need for a mass reconstruction, by

$$M_{ap} = \int d^2\theta Q(\theta)\gamma_t(\theta), \quad (5)$$

where  $Q(\theta)$  is given from  $U(\theta)$ :

$$Q(\theta) = \frac{2}{\theta^2} \int d\theta' U(\theta') - U(\theta). \quad (6)$$

The aperture mass variance is related to the convergence power spectrum eq. (1) by

$$\langle M_{ap}^2 \rangle(\theta_{ap}) = 2\pi \int dl l P_\kappa(l) \left[ \frac{12}{\pi(l\theta_{ap})^2} J_4(l\theta_{ap}) \right]^2, \quad (7)$$

where  $J_4$  is a fourth-order Bessel function of the first kind.

We compute the aperture mass variances from the shear correlation functions using relations eqs. (11) and (12). This approach has some advantages over direct measurement in that (i) it is the least affected by defects in the data, such as masking by bright stars, (ii) and it does not depend on the geometry of the data; (iii) thus it uses all information in the data (Hoekstra et al. 2002b). The two shear two-point correlation functions that are measured are:

$$\xi_{tt}(\theta) = \frac{\sum_{i,j}^{N_s} w_i w_j \gamma_{t,i} \gamma_{t,j}}{\sum_{i,j}^{N_s} w_i w_j}, \quad (8)$$

and

$$\xi_{rr}(\theta) = \frac{\sum_{i,j}^{N_s} w_i w_j \gamma_{r,i} \gamma_{r,j}}{\sum_{i,j}^{N_s} w_i w_j}, \quad (9)$$

where  $\theta = |x_i - x_j|$ ,  $N_s$  is the number of source galaxies,  $\gamma_t$  and  $\gamma_r$  are the tangential and 45° rotated shear in the frame connecting the pair of galaxies, and  $w$  is a weight that expresses the reliability of the shape measurement for each galaxy (discussed in §4). For the following discussion, it is useful to define,  $\xi_+(\theta)$  and  $\xi_-(\theta)$ , which are the sum and difference of the

shear two-point correlation functions defined by eqs. (8) and (9), respectively

$$\xi_+(\theta) = \xi_{tt}(\theta) + \xi_{rr}(\theta), \quad \text{and} \quad \xi_-(\theta) = \xi_{tt}(\theta) - \xi_{rr}(\theta). \quad (10)$$

The E and B modes' (which we denote by  $M_\perp$ ) aperture mass variances are derived by integration of these correlation functions with an appropriate window

$$\langle M_{ap}^2 \rangle(\theta_{ap}) = \pi \int_0^{2\theta_{ap}} d\theta \theta \left[ \mathcal{W}(\theta)\xi_+(\theta) + \tilde{\mathcal{W}}(\theta)\xi_-(\theta) \right], \quad (11)$$

and

$$\langle M_\perp^2 \rangle(\theta_{ap}) = \pi \int_0^{2\theta_{ap}} d\theta \theta \left[ \mathcal{W}(\theta)\xi_+(\theta) - \tilde{\mathcal{W}}(\theta)\xi_-(\theta) \right], \quad (12)$$

where  $\mathcal{W}$  and  $\tilde{\mathcal{W}}$  are given in Crittenden et al. (2002); useful analytical expressions were derived by Schneider et al. (2002).

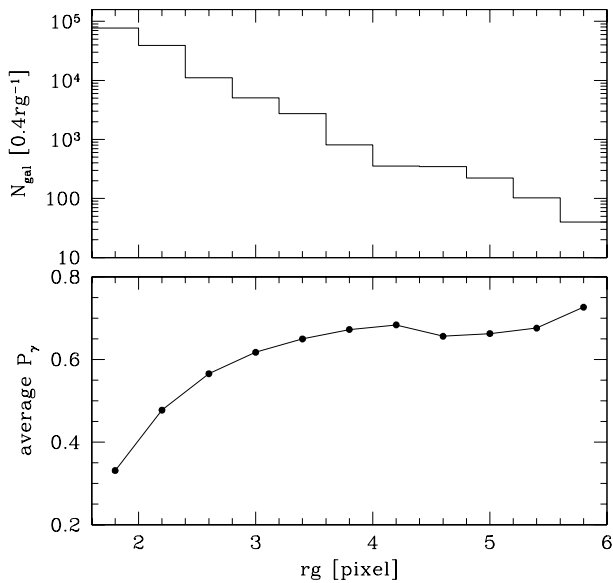


FIG. 1.— Top panel: the size distribution of objects used for the cosmic shear measurements. Bottom panel: Average  $\text{tr}(P_\gamma)$  as a function of  $rg$ .

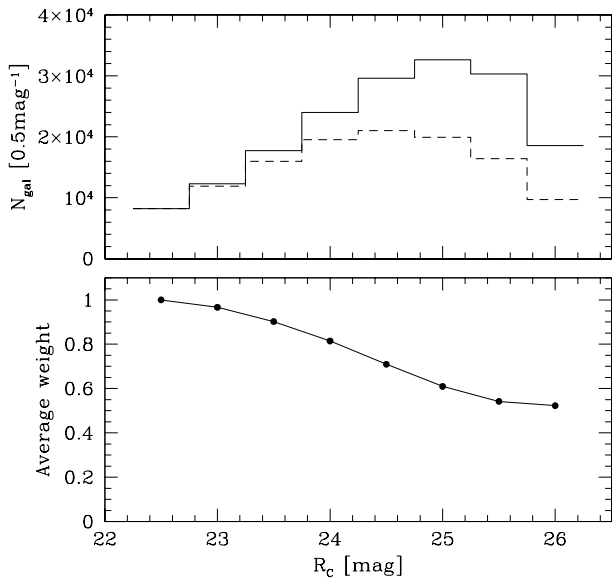


FIG. 2.— Top panel: the solid histogram shows the number counts of objects used for the cosmic shear measurements, while the dashed histogram is for the product of the number counts and the average weight. Bottom panel: Average weight as a function of  $R_C$  magnitude.

### 3. DATA

Observations were made with the Suprime-Cam on the Subaru 8.2-m telescope during its commissioning phase. We used a field size of  $2.1 \text{ deg}^2$ , which was the largest size possible during that period.

The field that we chose was centered at R.A. =  $16^h04^m43^s$ , decl. =  $+43^\circ12'19''$  (J2000.0). We obtained  $R_c$ -band images on the nights of 2001 April 23-25. Suprime-Cam has a field of view of  $34' \times 27'$  with a scale  $0''.202 \text{ pixel}^{-1}$  (see Miyazaki et al. 2002 for instrumental details of Suprime-Cam). Nine contiguous fields were observed in a  $3 \times 3$  mosaic configuration. Each exposure on a given field was offset by  $1 \sim 2'$  from the other exposures to allow the removal of cosmic rays and defects on the CCDs. The total exposure time of each field was 1800 sec ( $360 \text{ sec} \times 5$ ).

We apply the weak lensing mass reconstruction technique to these data (Miyazaki et al. 2002a). The number counts of high peaks (above  $5\text{-}\sigma$ ), which represent massive dark halos, in the reconstructed convergence field is  $4.9 \pm 2.3$ , where the Gaussian smoothing radius of the convergence map is  $1'$ . This result is consistent with predictions that assume the Press-Schechter mass function (Press & Schechter 1974; we used the version modified by Sheth & Tormen 1999) and the universal NFW halo profile (Navarro, Frenk & White 1996) under the cluster normalized CDM cosmology. Thus, it is unlikely that this field is significantly far from the cosmic mean.

The individual images were de-biased and then flattened using a median of all the object frames taken during the observing run. Stacking the dithered images is not a trivial procedure because of the large distortion in the optics, combined with the alignment error of each CCD with displacement and rotation from its nominal position. We present here an outline of how to obtain parameters that transform a CCD coordinate to a standard celestial coordinate. First, we employ a geometrical model of the field distortion using a fourth order polynomial function

$$\frac{R-r}{r} = ar + br^2 + cr^3 + dr^4, \quad (13)$$

where  $R$  and  $r$  are the distance from the optical axis in units of pixels on the face of the CCD and in celestial coordinates, respectively. We typically changed the telescope pointing by  $1 \sim 2$  arcmin between successive exposures to fill the gaps between the CCDs. The offset and rotation of the telescope pointing between the exposures are also set as free parameters. All of these parameters can be determined by minimizing the distance of the same stars identified on different exposures. To do this, we adopt a modified version of *mosaicfit*, which is one of the functions of the *imcat* suite.

Once we have obtained these parameters, we use them to warp each image before stacking. The residual of the distances between corresponding star images is a measure of the error of this mosaic-stacking procedure. The RMS value of the residuals is typically about 0.5 pixels. As shown in Miyazaki et al. (2002b), distortion parameters obtained in this way match quite well with the residuals predicted by optical ray-tracing programs, which implies that our solution is satisfactory.

The RMS residual of 0.5 pixels is due to several effects that are not considered in the simple model, including atmospheric dispersion and asymmetric aberration of the optics. We note, however, that the residual vector changes smoothly with position and can be well modeled as a third order bi-linear polynomial function of position. This model then gives a fine correction to our geometrical solution described above. The mea-

surements of the displacement and the warping of the images are carried out using *fitgeometry2* and *mosaicmap* of *imcat*, respectively, as described by Kaiser et al. (1999). As a result of these procedures, the final residual typically decreases down to 0.07 pixel RMS (14 milliarcsec). To derive a better astrometric solution, an external reference star catalog would have to be used. However, we simply employ each first exposure as a reference and accept the resulting moderate astrometric accuracy, as it does not significantly affect the weak lensing analysis. The individual images are then warped using the solution, and stacked. The seeing in the resulting image is  $0''.68$  FWHM and the scatter among the fields is quite small at  $0''.04$  rms.

To carry out object detection, photometry and shape measurements of objects, we use *hfindpeaks*, *apphot* and *getshapes* of the *imcat* suite, which are an implementation of Kaiser et al. (1995). Catalogs created for the nine fields are registered using stars in the overlapping regions to generate a final catalog whose total field of view is  $1.64^\circ \times 1.28^\circ$ . Differences in the photometric zero point among the fields due to variation in the sky conditions (in turn, due to thin cirrus and differing air mass) are compensated for at this stage, but the adjustment is not significant ( $\sim 0.05$  mag).

We adopt slightly different object selection criteria to those used by Miyazaki et al. (2002a) to optimize our cosmic shear correlation measurement. Our criteria are (i)  $22.5 < R_c < 26$ . (ii) The signal-to-noise (S/N) ratio,  $nu$ , calculated in *imcat*, exceeds 7 (Erben et al. 2001). (iii) The image size is larger than the PSF size,  $rg > 1.45 \sim 1.65$ , where  $rg$  is a measure of the size of objects (in pixel units) yielded by *imcat*. The PSF size is identified from the stellar branch in the size-magnitude ( $rg-R_c$ ) plane. The PSF size varies slightly from pointing to pointing because of changes in the seeing conditions. (iv) Objects with  $rh > 10$  pixels (where  $rh$  is the half light radius) are considered too large and removed. (v) Highly elliptical objects, where the observed ellipticity,  $|e^{obs}| > 0.5$ , are removed. (vi) Objects that have a close companion, with a separation of less than 10 pixels ( $\simeq 2$  arcsec), are removed to avoid the problem of overlapping isophotes reported by Van Waerbeke et al. (2000). The number of objects that pass these various selection criteria (i)-(vi) is 249,071 ( $32.9 \text{ arcmin}^{-2}$ ).

Van Waerbeke et al. (2000) reported that regions where data from different CCDs are stacked together as a result of offsets between exposures (specifically, the edges of CCDs) can potentially produce discontinuities in the properties of the field and thus make the PSF correction difficult. This effect could cause a systematic error in the cosmic shear correlation measurement. Therefore, we decided to mask such regions. That is, we use only objects that were observed by the same CCD. About 35% of the objects are removed by this masking, and the number of objects in the final catalog is 161,740. The image size distribution and magnitude distribution of the catalog are shown in the upper panel of Figure 1 and Figure 2, respectively.

#### 4. GALAXY SHAPE ANALYSIS

The observed ellipticity of galaxies is measured from the weighted quadrupole moments  $I_{ij}$  of the surface brightness  $f(\theta)$ :

$$e_{obs} = \left( \frac{I_{11} - I_{22}}{I_{11} + I_{22}}, \frac{I_{12}}{I_{11} + I_{22}} \right), \quad I_{ij} = \int d^2\theta W_G(\theta) \theta_i \theta_j f(\theta), \quad (14)$$

where  $W_G(\theta)$  is the Gaussian window function. Estimating the shear,  $\gamma$ , from the observed ellipticities,  $e_{obs}$ , involves two

steps: First, the point spread function (PSF) anisotropy is corrected using the star images as references,

$$e = e_{obs} - \frac{P_{sm}}{P_{sm}^*} e_{obs}^*, \quad (15)$$

where  $P_{sm}$  is the smear polarisability tensor, which is mostly diagonal (Kaiser et al. 1995).  $(P_{sm}^*)^{-1} e_{obs}^*$  was calculated for stars scattered over the field of view. We use unsaturated stars selected by the following criteria: (i)  $20.6 < R_c < 23.0$  (using fainter stars than this does not change the results, see the Appendix). Note that the saturation level identified from the size-magnitude ( $rg-R_c$ ) plane is  $R_c = 19.5 \sim 20.5$  which correlates with the seeing (with a fainter saturation level for a better seeing). (ii)  $nu > 15$ . (iii) The image size is within a narrow range of the seeing size,  $rg_* - 0.05 < rg < rg_* + 0.05$ , where  $rg_*$  denotes the central  $rg$  value (in pixel units) of the stellar branch in the  $rg-R_c$  plane.  $rg_*$  varies from pointing to pointing and is  $rg_* = 1.27 \sim 1.52$ . (iv) Highly elliptical objects, with an observed ellipticity,  $|e| > 0.3$ , are removed. As a result, the average number density of the selected stars is about  $1/\text{arcmin}^2$ , and there are on average about 60 stars in each chip. However, the chip-by-chip variation in the number of stars is quite large; some chips have only  $\sim 20$  stars because of the presence of a large saturated star in the field. We make the first order bi-polynomial fit to values of  $(P_{sm}^*)^{-1} e_{obs}^*$  as a function of position (a second order fit does not change the results, see the Appendix). To make this fit, we use the *efit* command in *imcat*, and flux weighting is not applied. This function is used in eq. (15) to correct the ellipticities of faint galaxies. This correction is made with the *ecorrect* command in *imcat*. Note that each CCD chip is treated independently in this procedure. We found that a first order fit corrects the PSF anisotropy well, and furthermore does not introduce a systematic artificial residual due to the wings of a higher order fit (Van Waerbeke et al. 2002), provided that overlapped CCD regions are masked. The RMS value of the ellipticities of the reference stars,  $(|e^*|^2)^{1/2}$ , is reduced from 2.8% to 1.0% as a result of the correction. Note that the RMS before the correction is already small, because of the superb image quality of the Subaru telescope. Figure 3 shows the star ellipticities before (left panel) and after (right panel) the anisotropic PSF correction from one pointing. The observed ellipticities not only have a large scatter but also show a systematic effect. After the PSF correction this tendency is removed and the corrected star ellipticities are distributed symmetrically around zero with a small scatter.

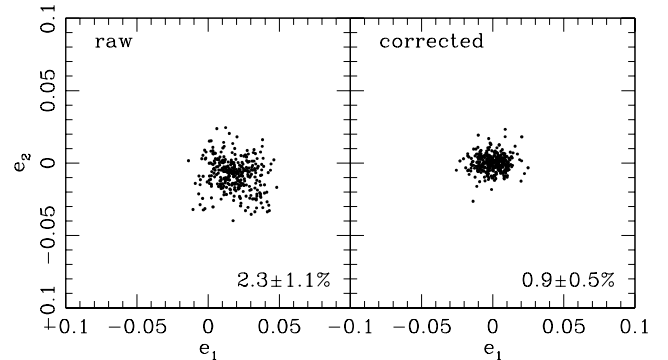


FIG. 3.— Ellipticities distribution of stars, before (left) and after (right) the correction for PSF anisotropies is made. The mean and dispersion of the ellipticities ( $|e|$ ) of all the stars are shown inside the frame.

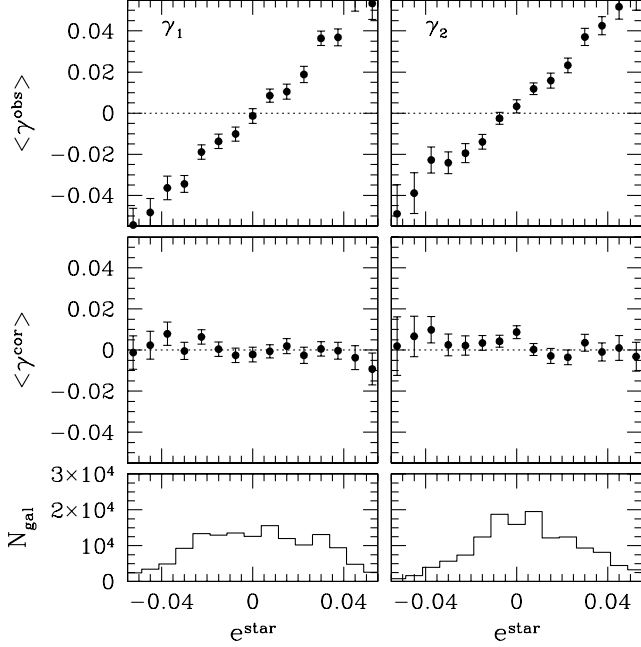


FIG. 4.— Components of galaxy ellipticities as a function of the star ellipticity component used for the anisotropic PSF correction. Top and middle panels show the averaged galaxy ellipticities before and after correction, respectively. Bottom panels show the ellipticity distribution of galaxies (number per bin) used for the cosmic shear correlation measurement.

Figure 4 shows the average ellipticity of galaxies as a function of the value of the star ellipticity used for the anisotropic PSF correction. The top panels show the observed ellipticities, and the expected strong correlation is present. Note that for the majority of galaxies, the PSF anisotropy is very small, as shown in the bottom panels. The corrected ellipticities plotted in the middle panels comprise only small values. The averaged values of the corrected ellipticities are  $\langle e_1 \rangle = -5.0 \times 10^{-4}$  and  $\langle e_2 \rangle = 1.8 \times 10^{-3}$ . Thus, no significant offset is found.

The second step is the isotropic correction, caused by the window,  $W_G$ , and the seeing. Luppino & Kaiser (1997) reported a method to correct the ellipticities for these effects. The *pre-seeing* shear  $\gamma$  is described as

$$\gamma = P_\gamma^{-1} e, \quad P_\gamma = P_{sh} - \frac{P_{sh}^* P_{sm}}{P_{sm}^*}, \quad (16)$$

where  $P_{sh}$  is the shear polarisability tensor. The  $P_\gamma$  of individual galaxies is, however, known to be a noisy estimate, and thus we adopt the smoothing and weighting method developed by Van Waerbeke et al. (2000; see also Erben et al. 2001 for a detailed study of the smoothing scheme). For each object, 20 neighbors are first identified in the  $r_g$ - $R_c$  plane. A median value of  $P_\gamma$  among these neighbors is adopted as the smoothed  $P_\gamma$  of the object. The averaged  $\text{tr}(P_\gamma)$  for all objects is calculated as 0.40 but  $P_\gamma$  depends on the object size. Figure 1 plots the averaged  $\text{tr}(P_\gamma)$  as a function of  $r_g$ . This graph shows that the average  $\text{tr}(P_\gamma)$  is almost constant,  $\sim 0.65$  for  $r_g > 3.5$ , but becomes smaller for smaller  $r_g$ .

As the estimated  $\gamma$  is still noisy, especially for small and faint objects, it is important to weight the galaxies according to the uncertainty in the shape measurements. We weight the objects using the procedure developed by Van Waerbeke et al. (2000; 2002; see also Erben et al. 2001). The variance of raw  $\gamma$  before the smoothing among the neighbors,  $\sigma_\gamma^2$ , is used to estimate the weight of each object,  $w$ , as

$$w = \frac{1}{\sigma_\gamma^2 + \alpha^2} \quad (17)$$

where  $\alpha^2$  is the variance of all the objects in the catalog and  $\alpha \simeq 0.4$  here. Under the weighting scheme, an averaged value of a certain observable,  $\langle A \rangle$ , is calculated as  $\sum_{i=1}^N w_i A_i / \sum_{i=1}^N w_i$  instead of  $\sum_{i=1}^N A_i / N$ . The lower panel of Figure 2 shows the averaged weight as a function of  $R_c$  magnitude. As expected, less weight is given to fainter objects because the shape measurements of these objects are noisier. The dashed histogram in the upper panel of Figure 2 plots the product of the number counts and the average weight and shows that the *effective* counts peak at  $R_c \sim 24.5$ .

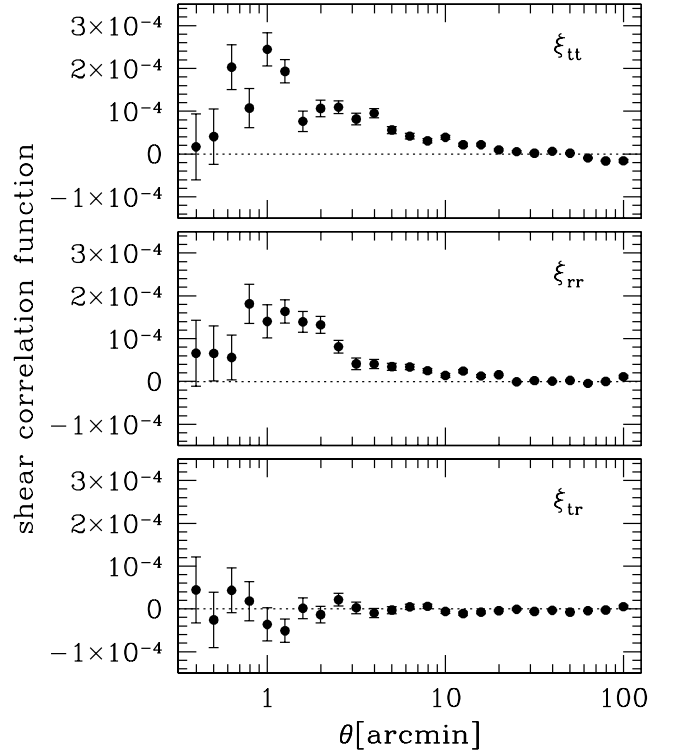


FIG. 5.— Shear correlation functions. Top panel is for  $\xi_{tt}$ , middle panel for  $\xi_{rr}$ , and bottom for the cross correlation  $\xi_{tr}$  which should vanish if the data are not contaminated by systematics. The error bars present the statistical error computed from 100 randomized realizations.

## 5. COSMIC SHEAR CORRELATIONS

In this section, we present the cosmic shear correlations measured from the 2.1 deg<sup>2</sup> Suprime-Cam data, and discuss their statistical and possible systematic errors.

The top and middle panels of Figure 5 show the shear correlation functions,  $\xi_{tt}$  and  $\xi_{rr}$ , respectively, computed using the estimator eqs. (8) and (9). The bottom panel presents the cross-correlation  $\xi_{tr}$ . The error bars indicate the RMS among 100 randomized realizations, in which the orientations of galaxies are randomized, and presumably represent the statistical error. In the following, statistical errors are computed in this manner. As the two top panels clearly show, we detect non-zero shear correlation signals on scales below 30 arcmin, except for the smallest two bins. On small scales ( $\theta < 1$  arcmin) the number of pairs corresponding to the separations decreases, and consequently the signals become noisy and the statistical errors become large. As the cross-correlation should be zero for a signal due to gravitational lensing, it provides a check on systematic effects in the data. The bottom panel shows that the cross-correlation is indeed consistent with zero at all scales. This result indicates

that our PSF corrections perform well and do not introduce a systematic effect into the data.

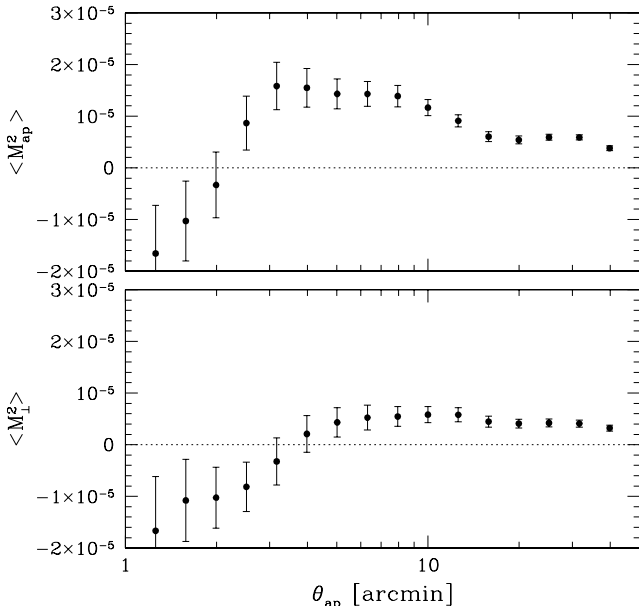


FIG. 6.— Upper panel shows the E-mode aperture mass variance  $\langle M_{ap}^2 \rangle$ , while the lower panel for B-mode aperture mass variance  $\langle M_{\perp}^2 \rangle$ . The error bars present the statistical error computed from 100 randomized realizations.

Let us now turn to the aperture mass variance. We compute the E and B mode aperture mass variances from the two-point shear correlation functions via eqs. (11) and (12). We use the analytic expressions for the window function  $\mathcal{W}$  and  $\tilde{\mathcal{W}}$  given in Schneider et al. (2002). The shear correlation functions defined by eq. (10) are computed over the range  $0.04' < \theta < 90'$  on 168 bins equally spaced with a log-interval of  $\Delta \log \theta = 0.02$ . The E and B mode aperture mass variances are plotted in Figure 6. For the E mode, we detect positive, non-zero signals on scales larger than  $\theta_{ap} > 2'$ . Since, as shown in Figure 5, the two-point correlation function becomes very noisy on scales smaller than 1 arcmin, and also considering that the aperture mass effectively probes a real scale of  $\sim \theta_{ap}/5$ , we use only the signals on scales larger than  $\theta_{ap} = 2$  arcmin for our maximum likelihood analysis in the next section. The amplitude and main features of the E mode variance are broadly consistent with theoretical predictions under the cluster normalized CDM cosmology (see Figure 8).

The B mode aperture mass variance is shown in the lower panel of Figure 6. Small but non-zero signals are found on scales larger than 5 arcmin. Currently, the origin of this B mode variance is not clear. One possibility is incorrect anisotropic PSF correction. We tested this possibility by repeating the PSF correction using different procedures, and found no significant problems (see the Appendix). It is interesting to note that Van Waerbeke et al. (2002) reported the detection in their data of a non-zero B mode variance ( $\langle M_{\perp}^2 \rangle \sim 3 \times 10^{-6}$ ) on scales  $10' < \theta_{ap} < 40'$ , the amplitude of which is very similar to ours. Note that their survey depth (a limiting magnitude of  $I_{AB} = 24.5$ ) was slightly shallower than ours. On the other hand, Hoekstra et al. (2002b) reported a vanishing B mode variance on scales larger than 10 arcmin in their shallow data ( $R_c < 24$ ). These results suggest that the current procedures for galaxy shape corrections become problematic for fainter objects. Unfortunately, we cannot test this possibility because the number of brighter

galaxies is not sufficient to obtain meaningful statistics. This possibility should be tested in future studies.

Currently, it is not clear how to correct the E mode variance, given the observed B mode. We follow Van Waerbeke et al. (2002b) and add the B mode in quadrature to the uncertainty in the E mode for the maximum likelihood analysis (see §6).

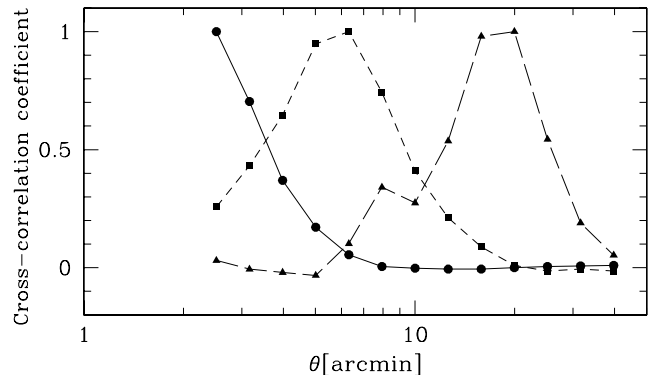


FIG. 7.— Cross-correlation coefficient  $r(\theta, \theta')$  for the statistical noise as a function of scale  $\theta$  for three scales,  $\theta' = 2.5$  (filled circles with solid line), 6.3 (filled squares with dashed line) and 20 arcmin (filled triangles with long-dashed line).

## 6. LIKELIHOOD ANALYSIS

In this section, we compare the measured aperture mass variance to the model predictions in CDM cosmologies using maximum likelihood analysis. We present constraints on cosmological parameters obtained from the cosmic shear variance observed in the Suprime-Cam 2.1 degree<sup>2</sup> field data.

### 6.1. Source redshift distribution

To compute the theoretical prediction of the aperture mass variance using eq. (7), we need to fix the redshift distribution of the source galaxies. However, no redshift information about the galaxies in our catalog is available. Therefore, we decided to adopt a parameterized model that provides a good fit to the redshift distribution of deep surveys (e.g., Hoekstra et al. 2002b; Van Waerbeke et al. 2002),

$$n_s(z) = \frac{\beta}{z_* \Gamma[(1+\alpha)/\beta]} \left(\frac{z}{z_*}\right)^\alpha \exp\left[-\left(\frac{z}{z_*}\right)^\beta\right], \quad (18)$$

with  $\alpha = 2$  and  $\beta = 1.5$ . The mean redshift relates to  $z_*$  as  $\bar{z}_s = z_* \Gamma[(2+\alpha)/\beta] / \Gamma[(1+\alpha)/\beta]$  and for these values of  $\alpha$  and  $\beta$ , it gives  $\bar{z}_s \simeq 1.5z_*$ . The median redshift is approximately given by  $z_{med} \simeq 1.4z_*$ . We treat the mean redshift of the distribution as a model parameter in the maximum likelihood analysis.

### 6.2. Maximum likelihood analysis

In performing the maximum likelihood analysis, we basically follow the procedure described in Van Waerbeke et al. (2002; see also Hoekstra et al. 2002b). The theoretical predictions are computed in a four-dimensional space, but we restrict the parameter space to realistic but conservative ranges:  $\Omega_m \in [0.1, 1]$  (either  $\Omega_\Lambda = 0$  or  $\Omega_m + \Omega_\Lambda = 1$ ),  $\sigma_8 \in [0.2, 2]$ ,  $\Gamma \in [0.05, 0.75]$  and  $\bar{z}_s \in [0.3, 2.5]$  with a sampling of  $19 \times 19 \times 11 \times 23$ . In what follows, we refer to this parameter range ( $\Omega_m, \sigma_8, \Gamma, \bar{z}_s$ ) as the *default prior* space. The model predictions are then interpolated with an oversampling fivefold higher in each dimension.

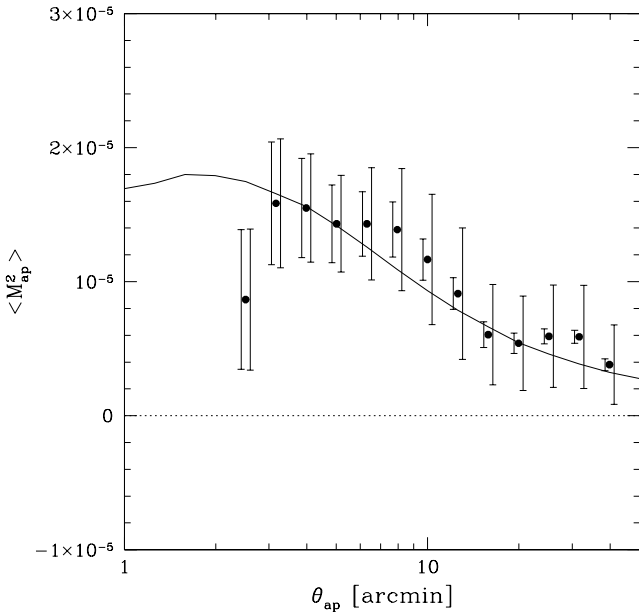


FIG. 8.— The aperture mass variance. For each measurement point, the left error bars show statistical error while right error bars present a sum of the statistical error, a residual systematic error estimated from B mode variance and the cosmic variance in quadrature. On smaller scales, statistical error dominates, while on larger scales residual error dominates. Comparing with them, the cosmic variance does not have a serious impact on the final error on all scales. The solid curve shows, for an illustrative example, the theoretical prediction of CDM model with  $\Omega_m = 0.3$ ,  $\Omega_\Lambda = 0.7$ ,  $\Gamma = 0.21$ ,  $\sigma_8 = 0.85$  and  $\bar{z}_s = 1$ .

For a given theoretical model, we compute the  $\chi^2$  (log-likelihood)

$$\chi^2 = (d_i - m_i)C^{-1}(d_i - m_i)^T, \quad (19)$$

where  $d_i$  is the measurement at scale  $\theta_i$ , and  $m_i$  is the corresponding theoretical prediction. Confidence values are computed from this  $\chi^2$  in the standard manner. The covariance matrix consists of three contributions

$$C(\theta_i, \theta_j) = C_s(\theta_i, \theta_j) + C_b(\theta_i, \theta_j) + C_{cv}(\theta_i, \theta_j), \quad (20)$$

where  $C_s$ ,  $C_b$  and  $C_{cv}$  are the statistical error, the residual systematics, and the cosmic variance, respectively, computed by the procedures described below. The statistical error was computed from the 100 randomized realizations catalog. Figure 7 shows the cross-correlation coefficient for the statistical noise for three scales, 2.5, 6.3, and 20 arcmin, with other scales. The non-zero B mode variance could indicate the existence of a residual systematic, although its origin is not yet clear. It would be natural to consider that a residual systematic of similar size also exists in the E mode. However, there is not yet a clear scheme to deal with this residual systematic. Therefore, we adopt the simple and conservative procedure described in Van Waerbeke (2002). We quadratically add the B mode variance to the error of the signal. As the E and B mode covariance matrices for the statistical noise are identical, the diagonal part of the matrix  $C_b$  is given by the B mode signal and off-diagonal terms follow the same correlation properties as the E mode.

Estimation of the cosmic variance is more complicated, because the observed scales are in the quasi-linear to nonlinear regime and thus random Gaussian theory cannot be applied. The cosmic variance is estimated using weak lensing numerical experiments, which are performed using a ray-tracing technique combined with large  $N$ -body simulations; the details are described in Hamana et al. (in preparation; see also Menard et al. 2003; Takada & Hamana 2003). Briefly, the dark matter

distribution from the observer ( $z = 0$ ) to high  $z$  ( $z \sim 3$ ) is generated by stacking 10 snapshot outputs from the  $N$ -body simulations.  $N$ -body data from the Very Large Simulation (VLS) which followed  $512^3$  particles in a cubic box of  $479h^1$ Mpc on a side, carried out by the Virgo Consortium (Jenkins et al. 2001; Yoshida, Sheth & Diaferio 2001) are used. A  $\Lambda$ CDM model ( $\Omega_m = 0.3$ ,  $\Omega_\Lambda = 0.7$  and  $h = 0.7$ ) is assumed with the CDM initial power spectrum computed using CMBFAST (Seljak & Zaldarriaga 1996). The multiple-lens plane ray-tracing algorithm is used to follow the light rays (Hamana & Mellier 2001, see also Jain, Seljak & White 2000 for the basic theory). The lensing convergence and shear is computed for  $1024^2$  pixels with a pixel size of 0.25 arcmin for a single source plane of  $z_s = 1$ . We compute the covariance matrix due to the cosmic variance from 36 random mock observations (but without the intrinsic ellipticity of galaxy images) generated by the numerical experiment. As the ratio of the non-Gaussian to Gaussian contributions to cosmic variance does not vary significantly with the underlying cosmology (Van Waerbeke et al. 2002), the cosmic variance also does not play an important role at all scales; given the large residual error from the B mode variance at large scales, we use the covariance matrix obtained from the  $\Lambda$ CDM numerical experiment regardless of the cosmological model considered. Figure 8 shows the aperture mass variance with error bars from the statistical error only (the left error bar on each point) and a sum of the statistical, systematic and cosmic variance in quadrature (the right error bar). On small scales, statistical error dominates [the statistical error (left) is comparable to the total error (right)], while at large scales the systematic error dominates given the large B mode variance.

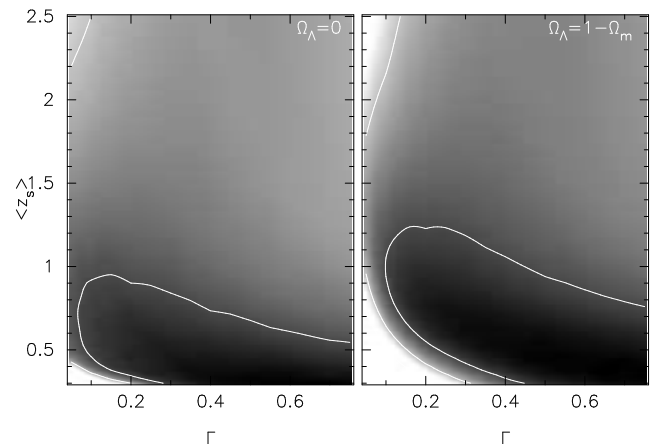


FIG. 9.— The gray-scale shows the  $\Delta\chi^2$  map on  $\Gamma$  and  $\bar{z}_s$  obtained after a marginalization over  $\Omega_m \in [0.1, 1]$  and  $\sigma_8 \in [0.2, 2]$ . A darker gray-scale indicates a lower  $\Delta\chi^2$  value (thus more likely). Contours indicate 68.3 and 95.4% confidence levels.

### 6.3. Results and discussion

Here, we present two-parameter space constraints obtained from marginalizations over the two remaining parameters. Figure 9 shows the likelihood map on the  $\Gamma$ - $\bar{z}_s$  plane where the default prior is applied for  $\Omega_m$  and  $\sigma_8$ . This Figure clearly presents the correlation between  $\Gamma$  and  $\bar{z}_s$ ; that is, a flatter (steeper) power spectrum (a larger (smaller)  $\Gamma$ ) prefers a lower (higher)  $\bar{z}_s$ , (this was reported previously by Van Waerbeke et al. 2002). The message here is that, given a relatively narrow range of signal detection ( $2' < \theta_{ap} < 40'$ ) with large error bars (as shown in Figure 8), the slope of the power spectrum and its normalization are degenerate. Similar considerations apply to a constraint on

$\sigma_8$ - $\Gamma$ , as shown in the lower left panel of Figure 10. Although the constraint on  $\Gamma$  and  $\bar{z}_s$  is not as tight, we can see from Figure 9 that for  $\bar{z}_s > 0.9$  ( $> 0.7$ ) a flatter power spectrum with  $\Gamma > 0.5$ , would be ruled out at more than the 68% confidence level for the flat (open) model.

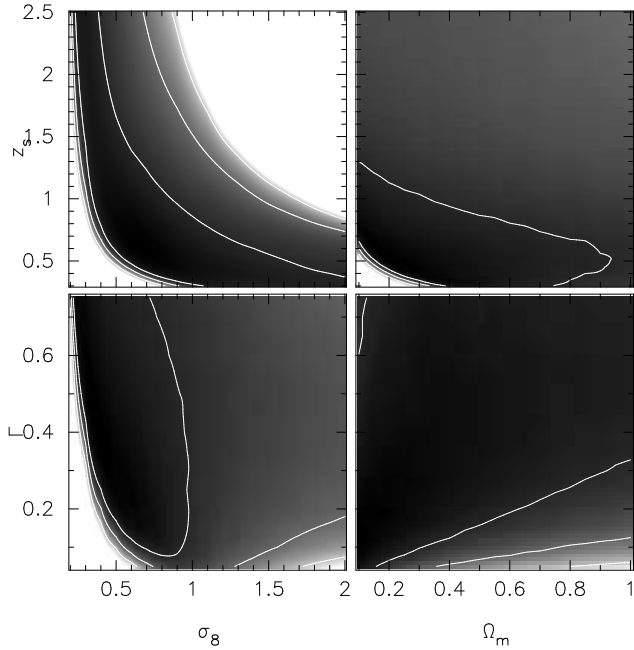


FIG. 10.— The gray-scale shows the  $\Delta\chi^2$  on two-parameter space obtained after a marginalization over two remaining parameters for the default prior, a darker gray-scale for a lower  $\Delta\chi^2$  value (thus more likely). Plots are for  $\sigma_8$ - $\bar{z}_s$  (upper left),  $\Omega_m$ - $\bar{z}_s$  (upper right),  $\sigma_8$ - $\Gamma$  (lower left) and  $\Omega_m$ - $\Gamma$  (lower right). Contours indicate 68.3, 95.4 and 99.73% confidence levels.

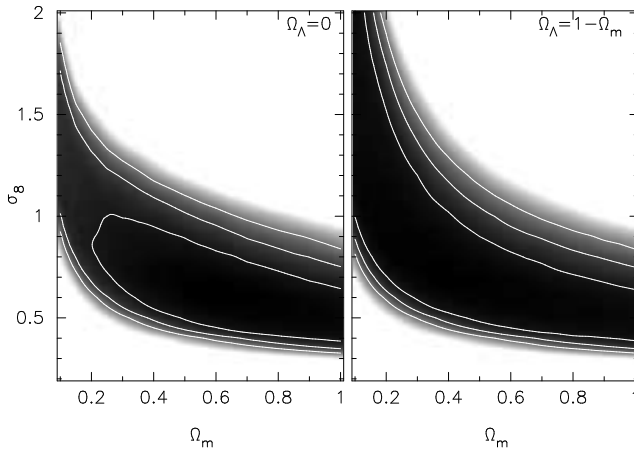


FIG. 11.— Constrains on  $\Omega_m$  and  $\sigma_8$  obtained after a marginalization over  $\Gamma \in [0.1, 0.4]$  and  $\bar{z}_s \in [0.6, 1.4]$ . Contours indicate 68.3, 95.4 and 99.73% confidence levels.

Figure 10 shows the degeneracy among the four parameters. The left panels clearly show the strong degeneracy between  $\sigma_8$  and  $\bar{z}_s$  (or  $\Gamma$ ). From these plots the following two points become clear: (i) redshift information about the source galaxies is crucial to obtaining a tight constraint on  $\sigma_8$  (Bernardeau et al. 1997; Jain & Seljak 1997). (ii) A constraint on  $\Gamma$  from other independent observations (such as galaxy clustering and/or CMB anisotropies) is very useful to break the degeneracy among the parameters. The right panels of Figure 10 show the same likelihood maps but for  $\Omega_m$ . The constraints on  $\Omega_m$  are weaker than those on  $\sigma_8$ , because the cosmic shear correlation is less sen-

sitive to  $\Omega_m$  than  $\sigma_8$  (Bernardeau et al. 1997; Jain & Seljak 1997).

In addition to the default prior, we adopt other priors from information obtained from other observations. We estimate the mean redshift of our galaxy catalog using redshift distributions from other deep surveys. The redshift distributions of faint galaxies in the Hubble Deep Fields North and South have been estimated using spectroscopic and photometric redshift techniques by several groups (Fernández-Soto et al. 1999; Cohen et al. 2000; Fontana et al. 1999; 2000; Yahata et al. 2000). Note that there is a small discrepancy between the two datasets, which is probably due to field-to-field variation. If we assume that our galaxy catalog has a similar redshift distribution to the Hubble Deep Field data, the mean redshift of our catalog ( $22.5 < R_c < 26$ ) is estimated to be larger than  $z = 1$ . On the other hand, the redshift distribution of galaxies in the Subaru deep survey field has been estimated using the photometric redshift technique with  $B V R_c i' z'$  data (Furusawa 2002; Furusawa et al. in preparation, see also Kashikawa et al. 2003). They found that the mean redshift of faint galaxies ( $R > 24$ ) is systematically lower than the HDF data. Note that the discrepancy is not very significant, given the large error bars due to small-number statistics. If we take the redshift distribution of the Subaru deep survey data, the median redshift of our catalog can be as low as  $z = 0.7$ . The difference between these two estimates suggests that the field-to-field variation can be quite large. It is also important to take into account that the weighting of galaxies might change the redshift distribution in a non-trivial manner. Considering these points, we adopt a conservative constraint of  $\bar{z}_s \in [0.6, 1.4]$ , and two tighter constraints of  $\bar{z}_s \in [0.6, 1.2]$  and  $\bar{z}_s \in [0.8, 1.4]$  to determine the impact of the source redshift information. We constrain  $\Gamma$  using the studies of galaxy clustering by the SDSS (Dodelson et al. 2002; Szalay et al. 2001) and the APM survey (Eisenstein & Zaldarria 2001). As there is a wide dispersion in  $\Gamma$  values among these studies, whereas the statistical error bars in each measurement are small, we adopt a conservative constraint,  $\Gamma \in [0.1, 0.4]$ , which covers the 68% confidence intervals of these three studies. We also take an extreme constraint of  $\Gamma = 0.21$ , where the 68% confidence intervals of the three studies overlap, to determine how well independent information on  $\Gamma$  improves the constraint on  $\Omega_m$  and  $\sigma_8$ .

Figure 11 shows the constraint on  $\Omega_m$  and  $\sigma_8$  obtained from marginalization over  $\Gamma \in [0.1, 0.4]$  and  $\bar{z}_s \in [0.6, 1.4]$ . As expected, a strong degeneracy between  $\Omega_m$  and  $\sigma_8$  is found. The confidence intervals of  $\Omega_m$  and  $\sigma_8$  from various priors are summarized in Table 1. It is clear from this Table that information about the redshift distribution of galaxies and  $\Gamma$  can indeed give a tighter constraint on  $\Omega_m$  and  $\sigma_8$ . Although the current constraint is not very tight, we may rule out the following two models. The COBE normalized high density CDM model (Bunn & White 1997, i.e.,  $\Omega_m = 1$ ,  $\Omega_\Lambda = 0$ ,  $\sigma_8 = 1.2$ ) is ruled out at more than the 99.9% confidence level. This model predicts too high an amplitude at all scales. For the open model, low density models with  $\Omega_m < 0.2$  are ruled out at more than the 68% confidence level. As pointed out by Van Waerbeke et al. (2002; see also Schneider et al. 1998), the incompatibility is because such low density models predict very large power at small scales. We obtain the following fitting function for the 95% confidence contours plotted in Figure 11,

$$\sigma_8 = (0.50_{-0.16}^{+0.35})\Omega_m^{-0.37}, \quad \text{for } \Omega_m + \Omega_\Lambda = 1, \quad (21)$$



TABLE 1

95.4% ONE-(TWO-)PARAMETER CONFIDENCE INTERVALS OBTAINED FROM THE APERTURE MASS VARIANCE,  $\Delta\chi^2 = 4.00$  (6.17), OF  $\Omega_m$  AND  $\sigma_8$  FOR DIFFERENT PRIORS. (...) INDICATES THAT NO CONSTRAINT IS PLACED WITHIN THE INTERVALS  $0.1 < \Omega_m < 1.0$  AND  $0.2 < \sigma_8 < 2.0$ .

$\langle z_s \rangle$	Priors		$\Omega_m + \Omega_\Lambda = 1$		$\Omega_\Lambda = 0$	
	$\Gamma$	$\Omega_m$	$\Omega_m$	$\sigma_8$	$\Omega_m$	$\sigma_8$
$\in [0.6, 1.4]$	$\in [0.05, 0.75]$	... (...)	...	$> 0.22$ (...)	$> 0.37$ ( $> 0.23$ )	0.22-0.93 ( $< 1.03$ )
$\in [0.6, 1.4]$	$\in [0.1, 0.4]$	... (...)	...	$> 0.29$ ( $> 0.26$ )	$> 0.41$ ( $> 0.26$ )	0.29-0.79 (0.26-0.86)
$\in [0.6, 1.4]$	0.21	... (...)	...	0.33-1.92 ( $> 0.31$ )	$> 0.43$ ( $> 0.26$ )	0.33-0.70 (0.31-0.76)
$\in [0.6, 1.2]$	$\in [0.05, 0.75]$	... (...)	...	$> 0.24$ ( $> 0.21$ )	$> 0.36$ ( $> 0.24$ )	0.23-0.93 (0.21-1.03)
$\in [0.6, 1.2]$	$\in [0.1, 0.4]$	... (...)	...	$> 0.31$ ( $> 0.29$ )	$> 0.40$ ( $> 0.25$ )	0.31-0.79 (0.29-0.87)
$\in [0.6, 1.2]$	0.21	... (...)	...	0.35-1.92 ( $> 0.33$ )	$> 0.43$ ( $> 0.28$ )	0.35-0.70 (0.33-0.76)
$\in [0.8, 1.4]$	$\in [0.05, 0.75]$	... (...)	...	0.21-1.65 ( $< 1.75$ )	$> 0.36$ ( $> 0.21$ )	0.21-0.76 ( $< 0.81$ )
$\in [0.8, 1.4]$	$\in [0.1, 0.4]$	... (...)	...	0.28-1.44 (0.25-1.56)	$> 0.39$ ( $> 0.22$ )	0.27-0.63 (0.25-0.68)
$\in [0.8, 1.4]$	0.21	... (...)	...	0.32-1.29 (0.31-1.39)	$> 0.41$ ( $> 0.23$ )	0.32-0.55 (0.31-0.61)

and

$$\sigma_8 = (0.51_{-0.16}^{+0.20})\Omega_m^{-0.34}, \quad \text{for } \Omega_\Lambda = 0. \quad (22)$$

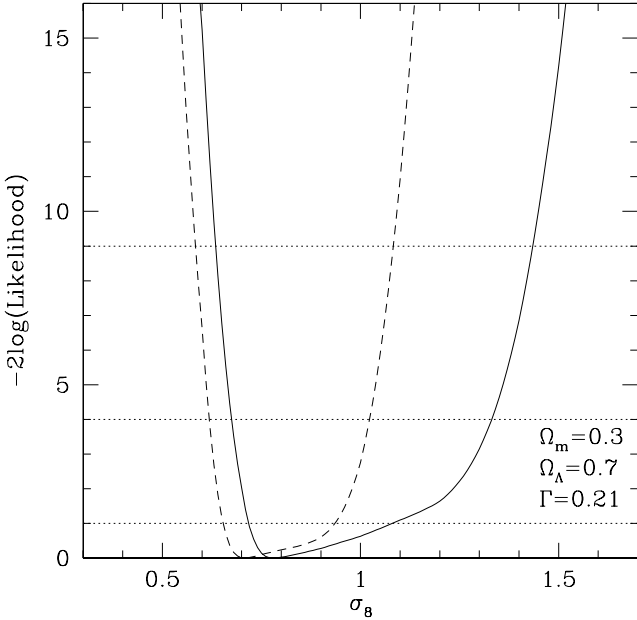


FIG. 12.— The one-dimensional likelihood function ( $\Delta\chi^2$ ) for  $\sigma_8$  in the flat  $\Lambda$ CDM cosmological model with  $\Omega_m = 0.3$  ( $\Omega_\Lambda = 0.7$ ) and  $\Gamma = 0.21$  for priors  $\bar{z}_s \in [0.6, 1.2]$  (the solid line) and  $\bar{z}_s \in [0.8, 1.4]$  (dashed line). The horizontal dotted lines indicate, from lower to upper, 68.3, 95.4 and 99.73% confidence levels.

Figure 12 shows the one-dimensional likelihood function for  $\sigma_8$  in the currently popular flat  $\Lambda$ CDM cosmological model with  $\Omega_m = 0.3$  ( $\Omega_\Lambda = 0.7$ ) and  $\Gamma = 0.21$ . The solid curve is for the prior  $\bar{z}_s \in [0.6, 1.2]$ , while the dashed curve is for  $\bar{z}_s \in [0.8, 1.4]$ . Specifically, the one-dimensional confidence intervals of  $\sigma_8$  for the 95.4% level are:  $0.68 < \sigma_8 < 1.33$  for  $\bar{z}_s \in [0.6, 1.2]$ ,  $0.62 < \sigma_8 < 1.02$  for  $\bar{z}_s \in [0.8, 1.4]$ , and  $0.62 < \sigma_8 < 1.32$  for  $\bar{z}_s \in [0.6, 1.4]$ . A strong degeneracy between  $\sigma_8$  and  $\bar{z}$  is evident. Especially, the upper bound of the  $\sigma_8$  confidence interval is very sensitive to the choice of the lower limit of the mean redshift. This is also seen in the upper left panel of Figure 10. From these results we may say that, for the flat  $\Lambda$ CDM cosmological model, we obtain a relatively reliable lower bound of  $\sigma_8 > 0.62$  (95.4% confidence) for a reasonable choice of  $\bar{z}_s$ . However, the upper limit is uncertain; it depends

strongly on the choice of the mean redshift. A conservative conclusion is  $\sigma_8 < 1.33$  (95.4% confidence), but it is tightened by  $\sigma_8 < 1.02$  if the mean redshift is as large as  $\bar{z}_s = 0.8$ .

Our results are broadly consistent with constraints obtained from other cosmic shear surveys (Maoli et al. 2001; Bacon et al. 2002; Van Waerbeke et al. 2002; Hoekstra et al. 2002b; Refregier, Rhodes & Groth 2002; Brown et al. 2003; Jarvis et al. 2003). This consistency is remarkable, given that the data have been compiled from different instruments, filters and survey depths. However, there is a spread of confidence intervals among the surveys. In fact, Bacon et al. (2002) and Van Waerbeke et al. (2002) obtained a slightly higher normalization,  $\sigma_8 \sim 0.95$  for the  $\Lambda$ CDM model, which is incompatible with our 68.3% confidence interval for  $\bar{z}_s \in [0.8, 1.4]$ . Note that Bacon et al. (2002) did not decompose the shear correlation function into E and B modes. Thus, their correlation function could be biased on the high side. The source of the small discrepancy among the cosmic shear surveys is unclear: it could be field-to-field variance, it could arise from the different analysis schemes, or it could be due to a mis-choice of the redshift distribution of galaxies. Hirata & Seljak (2003) investigated biases induced by the conversion between the observed image shape to shear distortion in current weak lensing analyses. They found that the non-Gaussianity of the point spread function has a significant effect and can lead to up to a 15% error in  $\sigma_8$  depending on the method of analysis. A wider field, multi-color survey, and an analysis scheme calibrated using mock observations (as reported by Erben et al. 2000) are needed to improve the accuracy of the cosmic shear analysis.

It is interesting to compare our results with the  $\sigma_8$  values obtained from the number density of rich clusters of galaxies published by many other groups. It should, however, be emphasized that there is a large dispersion in  $\sigma_8$  values among these studies, whereas the errors in each measurement are quite small. The  $\sigma_8$  values reported range from  $\sigma_8 \lesssim 0.7$  (e.g., Borgani et al. 1999; 2001; Seljak 2002; Vianna, Nichol & Liddle 2002) to  $\sigma_8 \gtrsim 0.9$  (e.g., Eke, Cole & Frenk, 1996; Kitayama & Suto 1996; 1997; Bahcall & Fan 1998; Pen 1998; Pierpaoli et al. 2001) for the standard  $\Lambda$ CDM model.

This spread may reflect mainly the uncertainty in the relation between the mass and X-ray temperature of clusters. If we take the prior of  $\bar{z}_s \in [0.6, 1.4]$ , both values are well within our 95.4% confidence interval. However, larger  $\sigma_8$  values are not preferred by the constraint obtained from the high- $\bar{z}_s$  prior,

but are well within the 95.4% confidence interval of the low- $\bar{z}_s$  prior. Thus, if the mean redshift of our galaxy catalog is as high as that estimated from the HDF data ( $\bar{z}_s \gtrsim 1$ ), our result is more in accord with the lower  $\sigma_8$  value.

Recently, Spergel et al. (2003) combined CMB measurements from WMAP (Bennet et al. 2003 and references therein), CBI (Person et al. 2002) and ACBAR (Kuo et al 2002), the galaxy power spectrum from the 2dF galaxy redshift survey (Percival et al. 2001; Verde et al. 2002), and the measurements of the Lyman  $\alpha$  power spectrum (Croft et al. 2002; Gnedin & Hamilton 2002) to find the best fit cosmological model and obtained  $\sigma_8 = 0.84 \pm 0.04$  (68% confidence). This result is in good agreement with our cosmic shear constraints.

## 7. SUMMARY

We analyzed the Suprime-Cam 2.1 deg<sup>2</sup>  $R_c$ -band data and measured the cosmic shear correlation. Suprime-Cam has a wide field of view of  $34' \times 27'$ , and its superb imaging quality provides a very small RMS value of star ellipticities of 2.8%, which after PSF corrections is reduced to 1.0%. These advantages combined with the large light gathering power of the 8.2-m Subaru telescope make Suprime-Cam an almost ideal camera for a weak lensing survey.

For the cosmic shear correlation measurement we used galaxies with  $22.5 < R_c < 26$  and an image size larger than the seeing size. We detected a non-zero cosmic shear two-point correlation function of up to  $40'$ . However, this result may be contaminated by shear that is not caused by gravitational lensing. We thus adopted the aperture mass variance, which naturally decomposes the correlation signal into E and B modes (the latter arises from shear whose origin is not in gravitational lensing).

We detected a non-zero E mode variance on scales from  $\theta_{ap} = 2'$  to  $40'$ . As the aperture mass probes a scale of  $\theta_{ap}/5$ , the signals come from effective scales of  $0.5' < \theta < 10'$ , corresponding to the quasi-linear to nonlinear regimes. We also detected a small but non-zero B mode variance on scales larger than  $\theta_{ap} > 5'$ . Currently, the origin of this B mode variance is not clear. One possibility is an incorrect anisotropic PSF correction. To test this possibility, we repeated the anisotropic PSF correction using different procedures (see the Appendix for details), namely: (i) a second order bi-polynomial fit to PSF, (ii) a pointing-by-pointing correction without masking overlapped regions and (iii) using fainter stars for modeling the PSF anisotropy. We did not find significant problems in our PSF correction procedure.

Interestingly, the amplitude of the B mode variance on larger scales is similar to that found by Van Waerbeke et al. (2002), though their survey depth was slightly shallower than ours. On the other hand, Hoekstra et al. (2002b) found a vanishing B mode variance on scales larger than 10 arcmin in their shallow data ( $R_c < 24$ ). These results may suggest that the current

procedures for galaxy shape correction become problematic for fainter objects. Future detailed studies of the origin of the B mode shear are required to understand and suppress this possible source of residual systematic error. Also, a calibration of the analysis scheme using mock data is needed to improve the accuracy of the cosmic shear analysis.

We performed a maximum likelihood analysis in a four-dimensional space of  $\sigma_8$ ,  $\Omega_m$ ,  $\Gamma$  and  $\bar{z}_s$ . We included three possible sources of error: the statistical noise, the cosmic variance, and the residual systematic estimated from the B mode variance. We derived joint constraints on two parameters by marginalizing over the two remaining parameters. We obtained a weak upper limit of  $\Gamma < 0.5$  for  $\bar{z}_s > 0.9$  (68% confidence). We also showed that independent information on  $\Gamma$  can reduce the degeneracy among the parameters. For the prior  $\Gamma \in [0.1, 0.4]$  and  $\bar{z}_s \in [0.6, 1.4]$ , we found  $\sigma_8 = (0.50^{+0.35}_{-0.16})\Omega_m^{-0.37}$  for  $\Omega_m + \Omega_\Lambda = 1$  and  $\sigma_8 = (0.51^{+0.29}_{-0.16})\Omega_m^{-0.34}$  for  $\Omega_\Lambda = 0$  (95.4% confidence). Although the current constraint is not very tight, we can rule out the following two models: the COBE normalized high density CDM model ( $\Omega_m = 1$ ,  $\Omega_\Lambda = 0$ ,  $\sigma_8 = 1.2$ ) by more than a 99.9% confidence level, and low density open models ( $\Omega_m < 0.2$ ) by more than 68% confidence. If we take the currently popular  $\Lambda$ CDM model ( $\Omega_m = 0.3$ ,  $\Omega_\Lambda = 0.7$ ,  $\Gamma = 0.21$ ), we obtain a one-dimensional confidence interval on  $\sigma_8$  for the 95.4% level,  $0.62 < \sigma_8 < 1.32$  for  $\bar{z}_s \in [0.6, 1.4]$ . This result is broadly consistent with constraints from other cosmic shear surveys and from the cluster abundance. However, we found that the confidence interval is sensitive to the choice of the mean redshift:  $0.68 < \sigma_8 < 1.33$  for the prior of  $\bar{z}_s \in [0.6, 1.2]$ , while  $0.62 < \sigma_8 < 1.02$  for  $\bar{z}_s \in [0.8, 1.4]$ . The latter is incompatible with the higher  $\sigma_8$  values obtained from some cluster abundance studies. This result clearly demonstrates that information on the redshift distribution of the source galaxies is crucial and can significantly tighten the confidence interval of  $\sigma_8$  and  $\Omega_m$ . The improvement of the constraint on  $\sigma_8$  from the redshift information can be estimated as follows: the cosmic shear correlation roughly scales with  $\sigma_8$  and the mean redshift as  $\xi \propto \sigma_8^{2.5} z_s^{1.5}$ , thus the uncertainty in the median redshift contributes to the error in  $\sigma_8$  as  $\delta\sigma_8/\sigma_8 = 0.6\delta z_s/z_s$ . Therefore, the error in  $\sigma_8$  due to uncertainty in the median redshift can be reduced to 10% by the current photometric redshift technique (e.g., Bolzonella, Miralles & Pelló 2000).

We would like to thank Y. Mellier for useful discussions and comments on the manuscript and L. Van Waerbeke for helpful discussions about galaxy shape analysis. We also thank the anonymous referee for detailed and constructive comments on an earlier manuscript, which improved the paper. T.H. thanks K. Umetsu and T. Futamase for useful discussions. T.H. F.N. and M.O. acknowledge support from Research Fellowships of the Japan Society for the Promotion of Science.

## REFERENCES

- Bacon, D. J., Refregier, A. R., & Ellis, R. S. 2000, MNRAS, 318, 625  
 Bacon, D. J., Massey, R. J., Refregier, A. R., & Ellis, R.S. 2002, submitted to MNRAS (astro-ph/0203134)  
 Bahcall, N. A., & Fan, X., 1998, ApJ, 504, 1  
 Bardeen, J., Bond, J., Kaiser, N., & Szalay, A. S., 1986, ApJ, 304, 15  
 Bartelmann, M., & Schneider, P., 2001, Phys. Rep., 340, 291  
 Bennett, C. L., et al., 2003, ApJ, submitted (astro-ph/0302207)  
 Blandford, R. D., Saust, A. B., Brainerd, T. G., & Villumsen, J. V., MNRAS, 251, 600  
 Bolzonella, M., Miralles, J.-M., & Pelló, R. 2000, A&A 363, 476  
 Borgani, S., Rosati, P., Tozzi, P., & Norman, C., 1999, A&A, 363, 476  
 Borgani, S., et al. 2001, ApJ, 561, 13  
 Brown, M. L., Taylor, A. N., Bacon, D. J., Gray, M. E., Dey, S., Meisenheimer, K., Wolf, C., 2003, MNRAS, 341, 100  
 Bunn, E. F., & White, M., 1997, ApJ, 480, 6  
 Cohen, J. G., Hogg, D. W., Blandford, R., Cowie, L. L., Hu, E., Songaila, A., Shopbell, P., Richberg, K., 2000, ApJ, 538, 29  
 Crittenden, R. G., Natarajan, P., Pen, U.-L., & Theuns, T., 2002, ApJ, 568, 20  
 Croft, R. A. C., Weinberg, D. H., Bolte, M., Burles, S., Hernquist, L., Katz, N., Kirkman, D., & Tytler, D. 2002, ApJ, 581, 20

- Dodelson, S., et al., (the SDSS collaboration), 2002, *ApJ*, 572, 140  
 Eisenstein, D. J., & Zaldarria, M., 2001, *ApJ*, 546, 2  
 Eke, V. R., Cole, S., & Frenk, C. S., 1996, *MNRAS*, 282, 263  
 Erben, T., van Waerbeke, L., Bertin, E., Mellier, Y. & Schneider, P., 2001, *A&A*, 366, 717  
 Fernández-Soto, A., Lanzetta, K. M., & Yahil, A., 1999, *ApJ*, 513, 34  
 Fontana, A., D'Odorico, S., Fosbury, R., Giallongo, E., Hook, R., Poli, F., Renzini, A., Rosati, P., & Viezzer, R., 1999, *A&A*, 343, L19  
 Fontana, A., D'Odorico, S., Poli, F., Giallongo, E., Arnouts, S., Cristiani, S., Moorwood, A., & Saracco, P., 2000, *AJ*, 120, 2206  
 Furusawa, H., 2002, Ph.D. thesis, Tokyo University  
 Gnedin, N. Y. & Hamilton, A. J. S. 2002, *MNRAS*, 334, 107  
 Hamana, T. & Mellier, Y. 2001, *MNRAS*, 169, 176  
 Hirata, C., & Seljak, U., 2003, *MNRAS* in press (astro-ph/0209489)  
 Hoekstra, H., Yee, H. K. C., Gladders, M. D., Barrientos, L. F., Hall, P. B., & Infante, L., 2002a, *ApJ*, 572, 55  
 Hoekstra, H., Yee, H. K. C., & Gladders, M. D., 2002b, *ApJ*, 577, 595  
 Hu, W., 1999, *ApJ*, 522, L21  
 Jain, B., & Seljak, U., 1997, *ApJ*, 484, 560  
 Jain, B. Seljak, U. & White, S. D. M. 2000, *ApJ*, 530, 547  
 Jarvis, M., Bernstein, G. M., Fischer, P., Smith, D., Jain, B., Tyson, J. A., Wittman, D. 2003, *AJ*, 125, 1014  
 Jenkins, A., Frenk, C. S., White, S. D. M., Colberg, J. M., Cole, S., Evrard, A. E., Couchman, H. M. P. & Yoshida, N. 2001, *MNRAS*, 324, 450  
 Kaiser, N., 1992, *ApJ*, 388, 272  
 Kaiser, N., Squires, G. & Broadhurst, T. 1995, *ApJ*, 449, 460  
 Kaiser, N., Wilson, G., Luppino, G., Dahle, H. 1999, *PASP*, submitted (astro-ph/9907229)  
 Kashikawa, N., et al., 2003, *AJ*, 125, 53  
 Kitayama, T., & Suto, Y., 1996, *ApJ*, 469, 480  
 Kitayama, T., & Suto, Y., 1997, *ApJ*, 490, 557  
 Kuo, C. L. et al. 2002, *ApJ*, submitted (astro-ph/0212289)  
 Luppino, G.A. & Kaiser, N. 1997, *ApJ*, 475, L20  
 Maoli, R., et al., 2001, *A&A*, 367, 766  
 Mellier, Y. 1999, *ARA&A*, 37, 127  
 Ménard, B., Hamana, T., Bartelmann, M., & Yoshida, N., 2003, *A&A*, 403, 817  
 Miralda-Escude, J., 1991, *ApJ*, 380, 1  
 Miyazaki, S., Hamana, T., Shimasaku, K., Furusawa, H., Doi, M., Hamabe, M., Imi, K., Kimura, M., Komiyama, Y., Nakata, F., Okada, N., Okamura, S., Ouchi, M., Sekiguchi, M., Yagi, M., & Yasuda, N., 2002, *ApJ*, 580, L97  
 Miyazaki, S., Komiyama, Y., Okada, N., Imi, K., Yagi, M., Yasuda, N., Sekiguchi, M., Kimura, M., Doi, M., Hamabe, M., Nakata, F., Shimasaku, K., Furusawa, H., Ouchi, M. & Okamura, S., 2002, *PASJ*, 54, 833  
 Navarro, J., Frenk, C. & White, S. 1996, *ApJ*, 462, 563  
 Peacock, J. A., & Dodds, S. J., 1996, *MNRAS*, 280, L19  
 Pearson, T. J. et al., *ApJ*, submitted (astro-ph/0205388)  
 Pen, U.-L., 1998, *ApJ*, 504, 601  
 Pen, U.-L., Van Waerbeke, L., Meller, Y., 2002, *ApJ*, 567, 31  
 Percival, W. J. et al., 2001, *MNRAS*, 327, 1297  
 Pierpaoli, E., Scott, D., White, M., 2001, *MNRAS*, 327, 1297  
 Press, W. & Schechter, P. 1974, *ApJ*, 185, 397  
 Refregier, A., Rhodes, J., & Groth, E. D., 2002, *ApJ*, 572, L131  
 Schneider, P., van Waerbeke, L., Jain, B. & Kruse, G. 1998, *MNRAS*, 296, 873  
 Schneider, P., van Waerbeke, L. & Mellier, 2002, *A&A*, 389, 729  
 Seljak, U., 2002, *MNRAS*, 337, 769  
 Seljak, U. & Zaldarriaga, M. 1996, *ApJ*, 469, 437  
 Sheth R. K., Tormen G., 1999, *MNRAS*, 308, 119  
 Spergel, D. N., et al. 2003, *ApJ*, submitted (astro-ph/0302209)  
 Szalay, A. S., et al., (the SDSS collaboration), submitted to *ApJ*, (astro-ph/0107419)  
 Takada, M., & Hamana, T. 2003, submitte to *ApJ*, (astro-ph/0305381)  
 Van Waerbeke, L. et al., 2000, *A&A*, 358, 30  
 Van Waerbeke, L. et al., 2001, *A&A*, 374, 769  
 Van Waerbeke, L. et al., 2002, *A&A*, 393, 369  
 Verde, L., et al., 2002, *MNRAS*, 335, 432  
 Vianna, P. T. P., Nichol, R. C., & Liddle, A. R., 2002, *ApJ*, 569, L75  
 Wittman, D. M., Tyson, J. A., Kirkman, D., Dell'Antonio, I., & Bernstein, G., 2000, *Nat*, 405, 143  
 Yahata, No., Lanzetta, K. M., Chen, H.-W., Fernández-Soto, A., Pascarella, S. M., Yahil, A., & Puetter, R. C., 2000, *ApJ*, 538, 493  
 Yoshida, N., Sheth, R. K. & Diaferio, A. 2001, *MNRAS*, 328, 669

## APPENDIX

## ANISOTROPIC PSF CORRECTION

In §5, we found a small but non-zero B mode aperture mass variance on scales larger than 5 arcmin. Currently, the origin of this B mode variance is not clear. One possibility is an incorrect anisotropic PSF correction. To test this possibility, we repeated the anisotropic PSF correction, but adopting different procedures:

1. use a second order bi-polynomial fit to  $(P_{sm}^*)^{-1} e_{obs}^*$ .
2. use the pointing-by-pointing correction without masking the overlapping regions.
3. use fainter stars for modeling the PSF anisotropy.

First, we repeated the anisotropic PSF correction adopting a second order bi-polynomial fit (the primary analysis uses a first order fit). In this case, we found that both the E and B mode aperture mass variances are almost identical to the results from our primary data, the differences are  $1 \times 10^{-6}$  at largest. Further, higher order fits are not feasible, because of the small number of stars in some chips. Note that Van Waerbeke et al. (2002) reported that a higher order polynomial fit to the PSF (third order in their case) caused a wing at the edge of fields and produced an artificial B mode signal.

Second, we applied the anisotropic PSF correction not to each chip separately but to each pointing, which is composed of ten chips (see Miyazaki et al. 2002 for instrumental details of Suprime-Cam). In this case, we did not mask the overlapping regions between different CCD chips that result from stacking dithering exposures. The second and fifth order bi-polynomial fits were adopted. No significant differences were found in either the E or B mode variances between the second and fifth order corrections. The E mode variance is consistent with our primary data (plotted in Figure 6). The amplitude of B mode variance is also similar to the primary data, but there is a bump at  $6' < \theta_{ap} < 15'$ . This scale is translated into a real scale of  $1' < \theta < 2'$ , which corresponds to the dithering angles between exposures. Thus, it is very likely that the bump arises from an inaccurate PSF correction at the overlapping regions where the PSF anisotropy pattern becomes very irregular<sup>9</sup>. Because of this result, we decided to mask the overlapping regions. Also, we decided to adopt the chip-by-chip correction to avoid poor modeling of the anisotropic PSF due to discontinuities between the chips.

Finally, we repeated the PSF correction but adopted slightly fainter stars to test the possibility of different responses to the PSF between bright and faint stars. Stars in the magnitude range  $21.5 < R_c < 23.5$  were used for the PSF correction with the first order fit ( $20.6 < R_c < 23.0$  for the primary procedure). The number of stars selected is almost the same as the primary selection ( $\sim 1/\text{arcmin}^2$ ). Both the E and B mode variance from these data are consistent with the primary data (specifically the results are within the error bars of the primary data). A much fainter criterion for star selection gives a poor PSF model because of contamination by small galaxies. Thus, it gives a very poor PSF correction.

<sup>9</sup> A similar B mode excess is found in CFHT data (L. Van Waerbeke & Y. Mellier, private communication).

In conclusion, as far as can be determined from the tests, we did not find a significant problem with our PSF correction procedure. A future detailed examination of the PSF correction method should be carried out using realistic simulation data, similar to the exercise performed by Erben et al. (2001). These tests, however, are beyond the scope of this paper and will be reported elsewhere.